RSC Advances

PAPER

View Article Online
View Journal | View Issue

Cite this: *RSC Adv.*, 2020, **10**, 4014

Coronary artery decision algorithm trained by two-step machine learning algorithm

Young Woo Kim,[a] Hee-Jin Yu,[a] Jung-Sun Kim,[b] Jinyong Ha,[c] Jongeun Choi*[a] and Joon Sang Lee *[a]

Received 1st November 2019
Accepted 17th January 2020

DOI: 10.1039/c9ra08999c

rsc.li/rsc-advances

A two-step machine learning (ML) algorithm for estimating both fractional flow reserve (FFR) and decision (DEC) for the coronary artery is introduced in this study. The primary purpose of this model is to suggest the possibility of ML-based FFR to be more accurate than the FFR calculation technique based on a computational fluid dynamics (CFD) method. For this purpose, a two-step ML algorithm that considers the flow characteristics and biometric features as input features of the ML model is designed. The first step of the algorithm is based on the Gaussian progress regression model and is trained by a synthetic model using CFD analysis. The second step of the algorithm is based on a support vector machine with patient data, including flow characteristics and biometric features. Consequently, the accuracy of the FFR estimated from the first step of the algorithm was similar to that of the CFD-based method, while the accuracy of DEC in the second step was improved. This improvement in accuracy was analyzed using flow characteristics and biometric features.

Introduction

Fractional flow reserve (FFR) is known as the gold standard for decision-making in coronary stenosis.[1] The primary advantage of FFR measurement is that it helps to avoid unnecessary stent insertion. The importance of FFR was confirmed by the FFR *versus* angiography for multivessel evaluation study, which demonstrated that an FFR-guided group exhibited significantly lower rates of major adverse effects compared with an angiography-guided group.[2] The pressure wire-based FFR, or the experimental FFR (FFR_{EXP}), is an original method for invasively measuring FFR. In this method, blood pressure at the proximal lesion and distal lesion of stenosis is directly measured using a wire;[3] however, the procedural time and expenses of FFR are not negligible, and there is a risk of complication because of adenosine injection.[4]

To overcome these problems, an FFR calculation technique based on computational fluid dynamics (CFD) has been developed. The CFD-based FFR calculation technique, or CFD-FFR, can avoid some invasive procedures by using geometric information from computed tomography (CT) or optical coherence tomography (OCT) images, along with the estimated or assumed boundary conditions. According to Coenen *et al.*, the accuracy of FFR_{CFD} is ~80% with a sensitivity of 87.5% and a specificity of 67.5%;[5] however, it requires expensive computational resources and a computational time of >8 h.[6]

Recently, to overcome the limitations of FFR_{CFD}, machine learning (ML) methods have been studied. Compared with the CFD method, ML can perform calculations in few minutes using lesser computational resources. Researchers from various medical fields are adopting ML for diagnosis and disease prediction. For example, Tripathy *et al.* performed a study on classification of breast cancer using cellular images with ML algorithm.[7] Moreover, Khanmohammadi *et al.* attempted to apply ML algorithm for diagnosing basal cell carcinoma *via* blood sample.[8]

Certain studies related to cell rheology such as the study by Kihm *et al.* used ML to classify cell types in blood.[9] Furthermore, attempts have been made to apply ML to estimate FFR. Kim *et al.* trained an ML model using intravascular ultrasound (IVUS) images to predict FFR and achieved an accuracy of 81%.[10] The limitations of their study were that the process was tedious and the segmentation of the IVUS image step was manual, which made it difficult to further increase the input data for the ML training. Another approach to address the lack of ML training data is to use a synthetic model. For example, Itu *et al.* generated a synthetic model of the circulatory system for ML training;[11] the model was generated by randomly extracting the characteristics of patient data. Then, CFD was used to calculate the FFR from these composite models. Compared with patient data, synthetic models can be infinitely amplified. Furthermore, because the features can be easily controlled, the uniformity of the data can be enhanced. Consequently, the ML model could estimate the FFR with the same accuracy as FFR_{CFD}; however,

[a]*Department of Mechanical Engineering, Yonsei University, Korea. E-mail: joonlee@yonsei.ac.kr; jongeunchoi@yonsei.ac.kr*

[b]*Division of Cardiology, Severance Cardiovascular Hospital, Yonsei University College of Medicine, Korea*

[c]*Department of Electrical Engineering, Sejong University, Korea*

this indicates that the accuracy of ML FFR is limited to that of FFR_{CFD}, which is 83% at maximum.

Tesche *et al.* and Hu *et al.* attempted to use synthetic models with other ML models to achieve an accuracy similar to that of the FFR_{CFD}.[12,13] Using ML-based FFR to increase the computational speed with accuracy constraints is an ineffective approach. The advantage of ML is the possibility of considering various features and determining their relationships. By maximizing the quality and quantity of the input features, the accuracy of ML-based FFR could surpass that of FFR_{CFD}.

In this study, a two-step ML algorithm for estimating both FFR and decision (DEC) is introduced. The primary purpose of this model is to suggest the possibility of ML-based FFR to be more accurate than FFR_{CFD}. For this purpose, a two-step ML algorithm that considers flow characteristics and biometric features as input features of ML is designed. Flow characteristics are the primary cause of pressure drop; thus, FFR is affected by both stenosis severity and flow characteristics. The relationship between the geometric features and FFR has been analyzed based on flow characteristics such as vorticity or turbulence intensity.[14,15] By providing flow characteristics as input parameters, the ML algorithm can have more information for increasing its accuracy.

Furthermore, regardless of the geometric features, biometric features can affect FFR. The limitation of CFD is the absence of a method that considers biometric features. Various attempts have been made to reflect biometric features, such as age or body mass index (BMI), in CFD;[16–18] however, these models are based on various assumptions and empirical equations that result in low accuracy. If these features can be analyzed using ML, the accuracy of ML-based FFR could surpass that of FFR_{CFD}. In this study, a two-step ML algorithm was developed to efficiently handle the flow characteristics and biometric features.

The summary of the algorithm process is shown in Fig. 1. This algorithm separately provides both estimated FFR and DEC. In the first step, the Gaussian progress regression (GPR) model is used to calculate FFR_{GPR}. In the second step, support vector machine (SVM) is used to calculate DEC_{SVM}.[19] The GPR model is trained from the CFD results of the synthetic model; therefore, the target accuracy of the FFR_{GPR} is the same as that of the FFR_{CFD}. However, the SVM model is trained by both FFR_{GPR} and flow characteristics and biometric features; therefore, the target accuracy of DEC_{SVM} should be higher than those of FFR_{GPR} or FFR_{CFD}.

This study focuses on categorizing and analyzing the mismatched cases of the two-step ML algorithm. Mismatch is defined as the wrong estimation of either FFR or DEC compared to FFR_{EXP} or DEC_{EXP}. To prove the need for the additional features, the flow characteristics and biometric features are analyzed for these mismatched cases.

Numerical methods

Lattice Boltzmann method

The lattice Boltzmann method is extensively used to solve microfluidics-related problems.[20–23] The Bhatnagar–Gross–Krook model with a single relaxation time is used to solve an incompressible fluid.[24] The governing equation with the forcing term can be written as follows:

$$f_i(x + e_i\Delta t,\ t + \Delta t) - f_i(x,t) = -\frac{1}{\tau}\left(f_i(x,t) - f_i^{eq}(x,t)\right) + \Delta t\left(1 - \frac{1}{2\tau}\right)\omega_i\left[\frac{e_i - u}{{c_s}^2} + \frac{e_i\cdot u}{{c_s}^4}e_i\right]\cdot f \quad (1)$$

with the following local equilibrium distribution function:

$$f_i^{eq} = \rho\omega_i\left[1 + \frac{1}{{c_s}^2}e_i\cdot u + \frac{1}{2{c_s}^4}(e_i\cdot u)^2 - \frac{1}{2{c_s}^2}u\cdot u\right] \quad (2)$$

where for the D3Q19 model,

$$\omega_i\begin{cases}\frac{1}{3}, & i = 0\\ \frac{1}{18}, & i = 1,2,\ldots,6\\ \frac{1}{36}, & i = 7,8,\ldots18\end{cases} \quad (3)$$

$$e_i\begin{cases}(0,0,0), & i = 0\\ (\pm1,0,0),(0,\pm1,0),(0,0,\pm1) & i = 1,2,\ldots,6\\ (\pm1,\pm1,0),(\pm1,0,\pm1),(0,\pm1,\pm1) & i = 7,8,\ldots18\end{cases} \quad (4)$$

In eqn (1), the density distribution function $f_i(x,t)$ indicates the proportion of particles moving with the i-th lattice velocity at lattice site x and time t; Δt is the time step; τ is the particle relaxation time; e_i is the discrete microscopic velocity; f_i is the local equilibrium distribution function; and $c_s = (c/\sqrt{3})$ is the speed of sound with $c = (\Delta x/\Delta t)$. The fluid density ρ and velocity u can be calculated using the following formula:

$$\rho = \sum_i f_i, \quad \rho u = \sum_i f_i e_i \quad (5)$$

The kinematic viscosity of plasma is given as follows:

$$v = \left(\tau - \frac{1}{2}\right){c_s}^2\Delta t \quad (6)$$

Moreover, the local shear stress and local dynamic viscosity can be calculated as follows:

$$\tau_{y,x}(\boldsymbol{x},t) = \left(1 - \frac{\tau}{2}\right)\sum_i\left(f_i(\boldsymbol{x})f_i^{eq}(\boldsymbol{x})\right)c_{yi}c_{xi} \quad (7)$$

$$\mu = \frac{\mathrm{d}u}{\mathrm{d}y}\frac{1}{\tau_{y,x}} \quad (8)$$

The inlet boundary condition of the simulation was given as the pulsatile pressure inlet, with a maximum pressure and minimum pressure were obtained from the patient information. Also, for the outlet boundary condition, the Windkessel model was used to reflect the compliance of the blood vessel, which was estimated from the height, BMI, and age of the

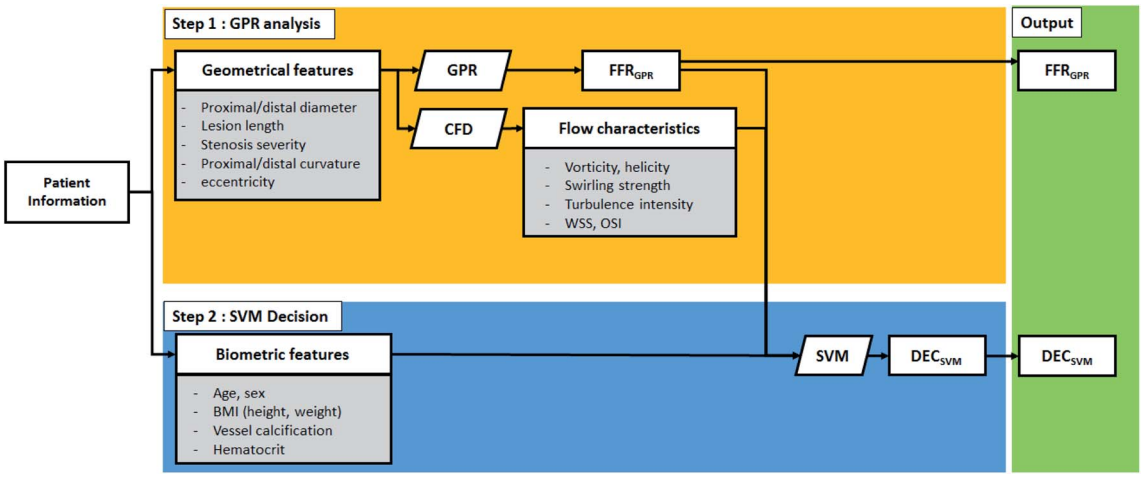

Fig. 1 Schematic of the two-step algorithm process.

patients. Note that for the synthetic models, the inlet and outlet parameters are randomized.

Biometric data and OCT-CT fusion image

The 3D image of the vessel for each patient can be obtained by reconstructing OCT and CT images. As reference, the FFR_{EXP} of a patient is measured using a pressure wire. Moreover, DEC_{EXP} is defined to have the value of 1 when stent surgery is required (FFR < 0.8) and 0 when it is not required (FFR ≥ 0.8). Furthermore, various biometric features, such as age, BMI, calcium score, and hematocrit, are collected along with the vessel geometry and FFR_{EXP}. The selection of the base 3D image for CFD analysis is important as geometric characteristics, such as resolution or curvature, can affect the FFR.[25,26] Both the OCT and CT images are merged to obtain an OCT-CT fusion image, as shown in Fig. 2. While OCT can obtain a high-resolution image of the lumen, the curvature of the vessels cannot be measured by this method. By fusing two images, more reliable

Table 1 Geometric features and their average, minimum, and maximum values

	Average	Minimum	Maximum
Total length (mm)	3.8	1.7	7.3
Proximal area (mm^2)	0.81	0.54	0.94
Center area (mm^2)	0.73	0.48	0.97
Distal area (mm^2)	0.76	0.53	0.94
Total curvature (degree)	21	0	90
Cross section eccentricity (%)	31	4	78

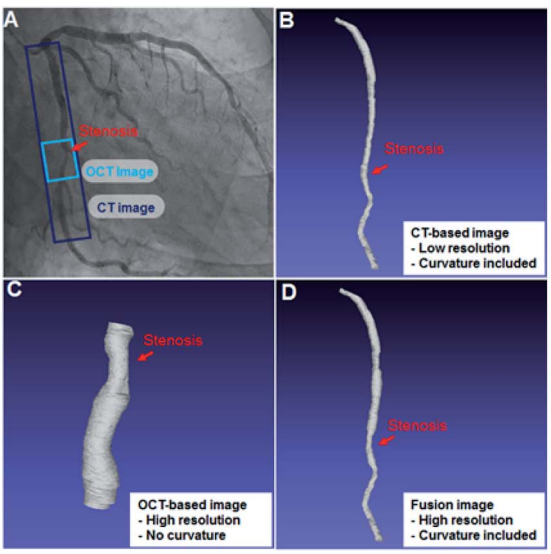

	FFR$_{OCT}$	FFR$_{CT}$	FFR$_{Fusion}$
Accuracy	82.8	75.3	87.1
Sensitivity	83.3	86.1	83.3
Specificity	82.5	68.4	89.5
PPV	75.0	63.3	83.3
NPV	88.7	88.6	89.5

Fig. 2 (Left) Examples of OCT, CT, and fusion images: (A) original CT image of patient (the ranges of CT image and OCT image measured are shown); (B) 3D model from CT with low resolution but with curvature; (C) OCT image with high resolution but without curvature; and (D) OCT-CR fusion image with both high resolution and curvature. (Right) Accuracy of FFR calculated by LBM method with each image types.

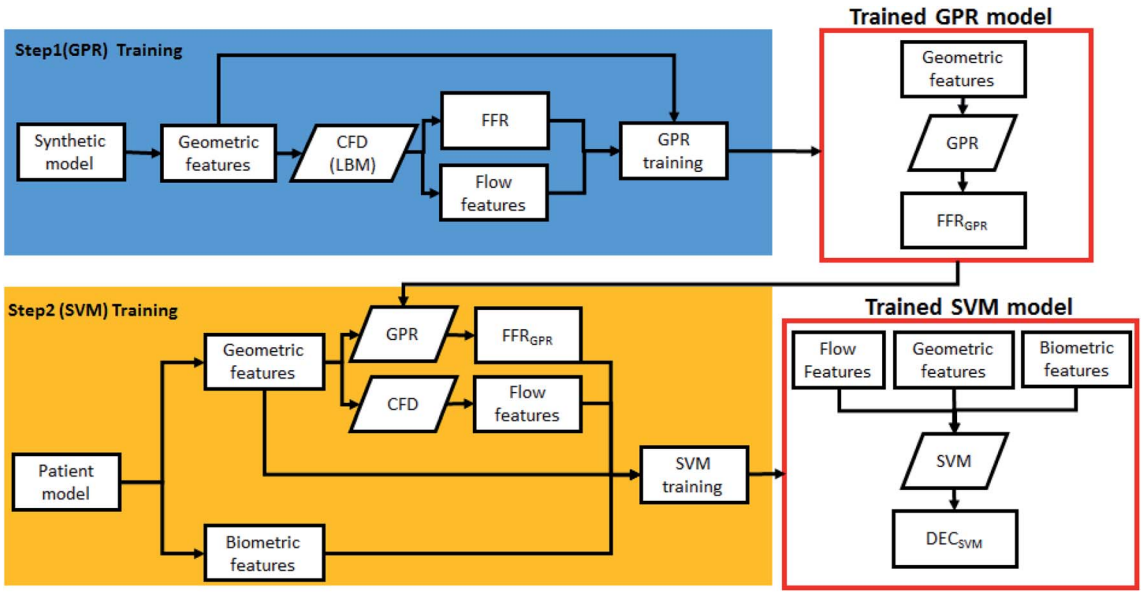

Fig. 3 Schematic of the two-step algorithm training process.

information about coronary stenosis can be obtained by the contribution of the delicate vessel curvature of the coronary CT image and the precise lumen contour of the OCT image.

For ML training, geometric features are extracted from the OCT-CT fusion image. The extracted features are diameter; length; the curvatures of the proximal, central, and distal segments of the lumen; and the cross section eccentricity. Table 1 lists the geometric features and their average, minimum, and maximum values.

Also, the synthetic vessel model is generated to amplify the quantity of data required for training the ML algorithm. The

Table 3 Diagnostic performance of each model for 20 patient cases. All units of values are given in percentage (%). PPV = positive predictive value, and NPV = negative predictive value

	FFR_{CFD}	FFR_{GPR}	DEC_{SVM}
Accuracy	65	65	75
Sensitivity	70	70	50
Specificity	60	60	80
PPV	75	75	83
NPV	25	25	64

Table 2 Performance of two-step algorithm with 20 patient cases

Number	Patient ID	FFR_{EXP}	DEC_{EXP}	FFR_{CFD}	FFR_{GPR}	DEC_{SVM}	Category
1	F155	0.38	1	0.722	0.723	1	1 (matched)
2	F187	0.53	1	0.624	0.622	1	
3	F172	0.71	1	0.767	0.773	1	
4	F200	0.78	1	0.696	0.701	1	
5	F134	0.79	1	0.704	0.698	1	
6	F194	0.85	0	0.842	0.838	0	
7	F87	0.86	0	0.904	0.906	0	
8	F133	0.87	0	0.823	0.819	0	
9	F18	0.9	0	0.901	0.901	0	
10	F176	0.91	0	0.847	0.844	0	
11	F201	0.94	0	0.926	0.928	0	
12	F152	0.88	0	0.752	0.745	0	2 (only SVM matched)
13	F188	0.88	0	0.782	0.784	0	
14	F159	0.90	0	0.759	0.763	0	
15	F198	0.77	1	0.789	0.8140	1	
16	F178	0.79	1	0.799	0.7942	0	3 (only GPR matched)
17	F163	0.78	1	0.799	0.7920	0	
18	F136	0.6	1	0.86	0.8537	0	4 (mismatched)
19	F116	0.77	1	0.829	0.8291	0	
20	F168	0.94	0	0.760	0.7512	1	

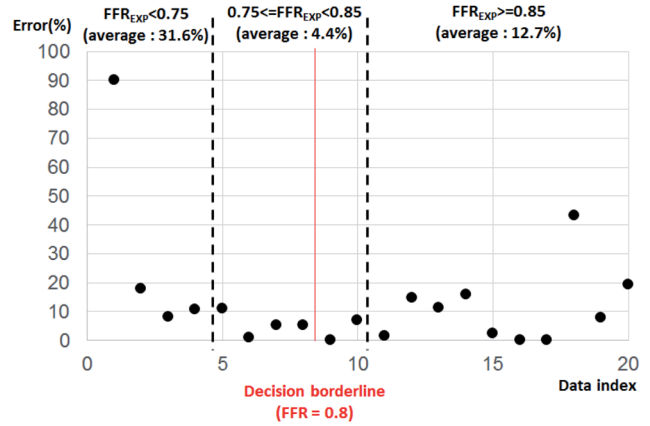

Fig. 4 Error percentage by data index aligned by FFR_{EXP}. The average error percentage was 27.46% when $FFR_{EXP} < 0.75$, 3.80% when $0.75 \leq FFR_{EXP} < 0.85$, and 12.70% when $FFR_{EXP} \geq 0.85$.

synthetic model is generated using the same geometric features extracted from the OCT-CT fusion image. Each value was randomized within a range of maximum/minimum values from patient data. Moreover, the biometric values used in fluid or boundary conditions were randomized. Table 1 lists the exact range of values of each parameter. The synthetic models are used to train the first step of our two-step algorithm.

Two-step ML algorithm training process

Fig. 3 shows the overall method of training the two-step ML algorithm. In summary, the first step is to train the GPR model using the synthetic model, while the second step is to train the SVM model with patient data. Each models are selected by considering the quality of input data (distance of data and outliers), along with model tests.

GPR is able to statistically model and predict an arbitrary smooth function even with small number of observations.[27–30] A Gaussian progress (GP) is a set of random variables which have a joint Gaussian distribution for any finite number of them. If $\{f(x), x \in R^d\}$ is a GP, then given n observations $x_1, x_2, \ldots, x_n$, the joint distribution of the random variables $f(x_1), f(x_2), \ldots, f(x_n)$ is Gaussian. A GP is defined by its mean function $m(x)$ and covariance function $k(x,x')$, which becomes:

$$E(f(x)) = m(x) \tag{9}$$

$$E[\{f(x) - m(x)\}\{f(x') - m(x')\}] = k(x,x') \tag{10}$$

From the model $h(x)^T\beta + f(x)$, where $f(x)$ are from a zero mean GP with covariance function, or $f(x) \sim GP(0, k(x,x'))$. $h(x)$ are a set of basis functions that transform the original feature vector x in R^d into a new feature vector $h(x)$ in R^p. β is a p-by-1 vector of basis function coefficients. This model represents a GPR model. An instance of response y can be modeled as

$$P(y_i|f(x_i),x_i) \sim N(y_i|h(x_i)^T\beta + f(x_i), \sigma^2) \tag{11}$$

SVM is a widely used classifier that uses supervised machine learning methods.[31,32] The purpose of the SVM is to construct an optimal hyperplane that separates the sample into its maximum margins. The SVM handles the classification of nonlinear data by nonlinear mapping the input space to the higher dimensional feature space using the appropriate kernel.[33]

The major advantage of SVM is that it guarantees the global optimality.[34] Let there be N data points $\{(x_i, y_i)\}_{i=1}^N$, where $x_i \in \mathbb{R}^m$ is the ith feature vector, and $y_i \in \{-1, +1\}$ is ith class label. Then, the hyperplane decision function $f(x) = \mathrm{sgn}((w^Tx) + b)$, where w is a weight vector and b is a bias, can be expressed as

$$f(x) = \mathrm{sgn}\left(\sum_{i=1}^{n} y_i\alpha_i(K(x, x_i) + b)\right) \tag{12}$$

where $K(x,x_i)$ is the symmetric nonnegative kernel function and $\alpha_i \geq 0$ is Lagrange multipliers. In this paper, we decided to use the Radial Basis Function (RBF) kernel through a comparison of the results for various kernels, which is defines as

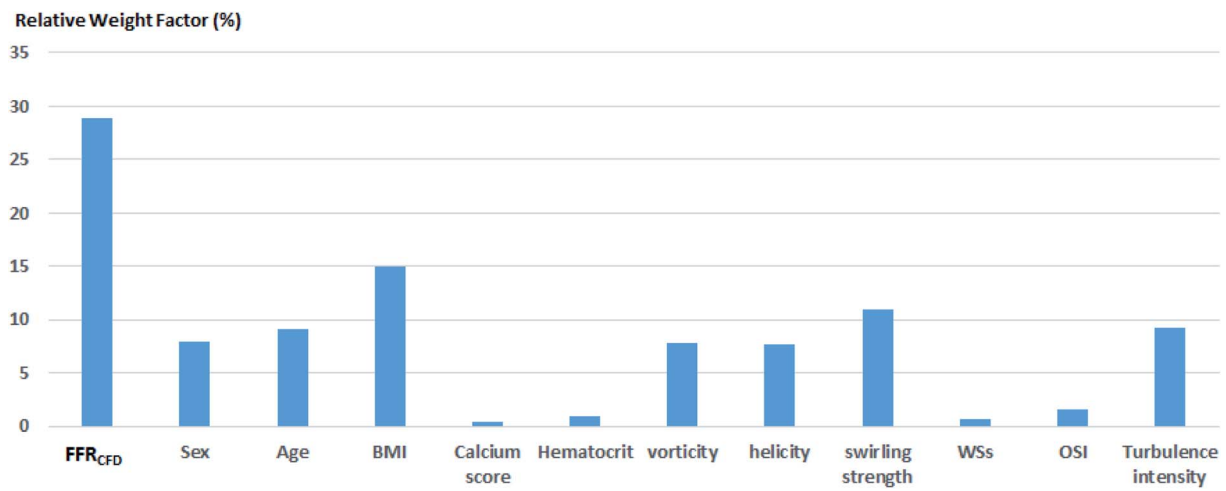

Fig. 5 Relative weight factors for each feature.

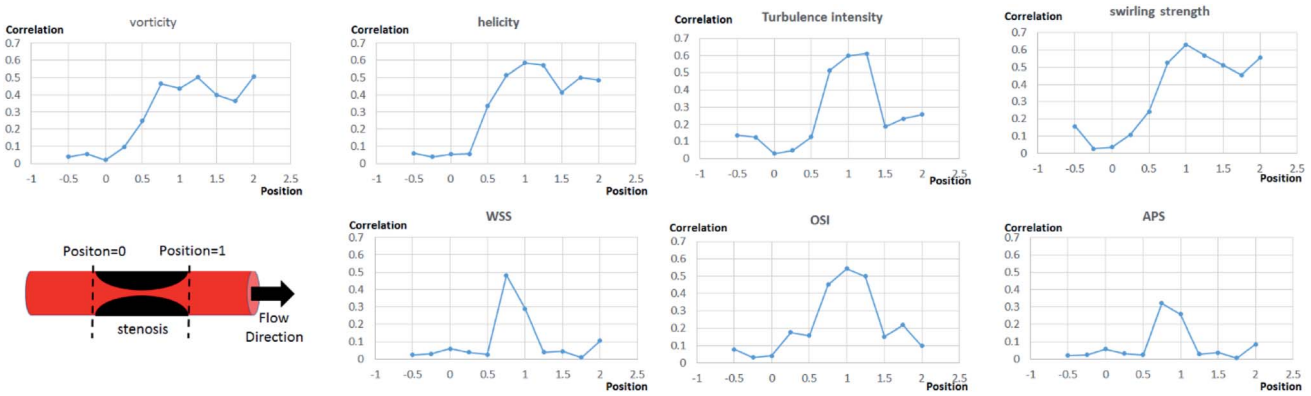

Fig. 6 Correlation between each flow features and FFREXP. The position between −1 and 0 is the proximal lumen, that between 0 and 1 is the center lumen, and that between 1 and 2.5 is the distal lumen.

$$K(\boldsymbol{x}, \boldsymbol{x}_i) = \exp\left(\frac{\|-\boldsymbol{x} - \boldsymbol{x}_i\|^2}{2\sigma^2}\right) \quad (13)$$

Features used in this study consist of biometric features including age, BMI, vessel calcification, *etc.* and dynamic features related to flow characteristics including vorticity, helicity, OSI, *etc.* Each flow characteristic has 11 points along the direction of the length of the vessel. Using these points, dynamic features were made by considering raw data, max/min value, max/min index, differences between points, derivatives, max/min value/index of derivatives, and area under the curve. A set of 94 features is extracted from each of the six flow characteristics and 14 demographic features are added to create a total of 580 features.

Also, before training SVM model, feature selection is performed. Feature selection is an essential technique in machine learning. Highly correlated, irrelevant features increase operation time and computational load and have a negative impact on performance. Feature selection techniques can be used to prevent overfitting and to improve model performance with minimizing variance and maximizing model the generalizability of the model. In this paper, Boruta is employed as the feature selection method. Boruta is an all-relevant feature selection method and one of the wrapper algorithms on the Random Forest.[35] It works through the following procedure:

(1) Add copies of all features to data set and shuffle them (which are called shadow features.)

(2) Train the Random forest classifier for extended data set and gather the feature importance scores that are Z scores.

(3) Check the importance of real features by comparing the Z scores of real features to the maximum Z score of the shadow feature and remove real features with lower Z scores.

(4) Repeat the process until the importance is assigned to all features, or until the algorithm reaches a specifically set limit for the Random forest runs.

The result of the Boruta algorithm is to divide the features into confirmed and rejected.

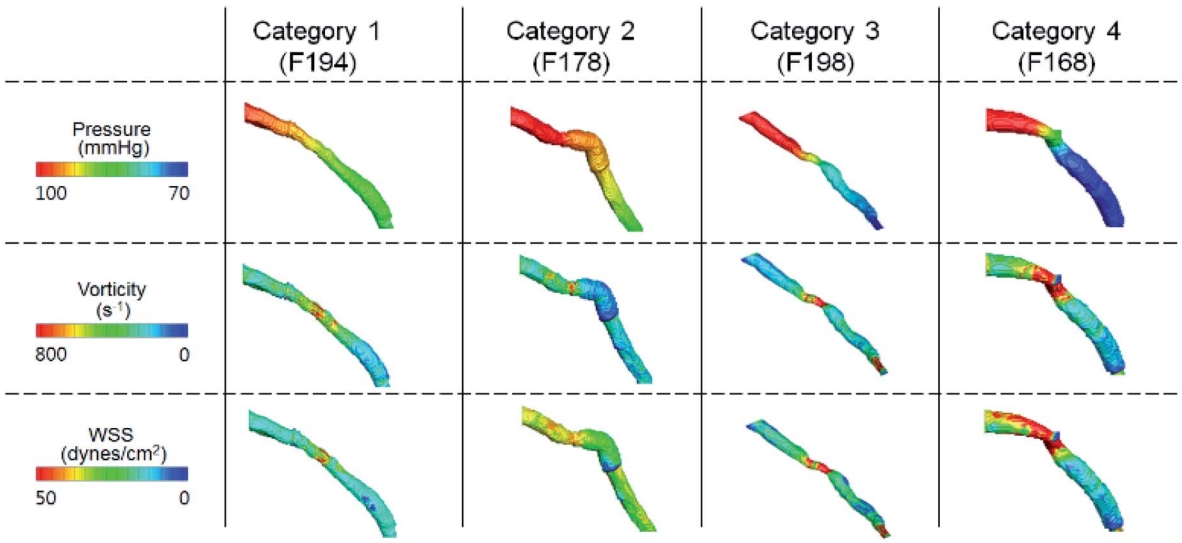

Fig. 7 Pressure, vorticity, and WSS of sample cases from each category.

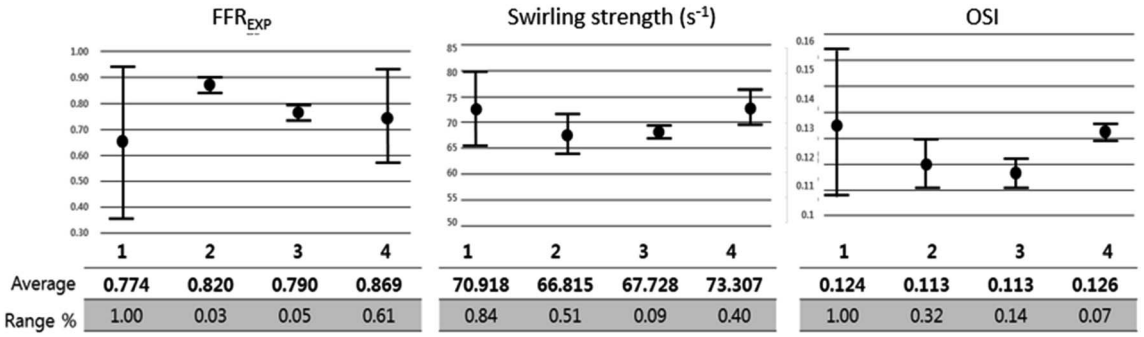

	1	2	3	4	1	2	3	4	1	2	3	4
Average	0.774	0.820	0.790	0.869	70.918	66.815	67.728	73.307	0.124	0.113	0.113	0.126
Range %	1.00	0.03	0.05	0.61	0.84	0.51	0.09	0.40	1.00	0.32	0.14	0.07

Fig. 8 FFR_{EXP}, vorticity, and WSS of 20 cases separated into four categories.

Results

ML result

Twenty patient cases were used to test the trained two-step algorithm. Table 2 presents the ML result. As seen in the table, the result cases are categorized into four types for further analysis: category 1 comprises the matched cases between experimental results and the algorithm for both FFR_{GPR} and DEC_{SVM}; category 2 comprises the cases that FFR_{GPR} mismatched but DEC_{SVM} matched; category 3 comprises cases where FFR_{GPR} is matched but DEC_{SVM} is mismatched; and category 4 is the case where both that FFR_{GPR} and DEC_{SVM} are mismatched. In terms of the two-step algorithm, category 2 is the most important one because it indicates that the two-step algorithm could determine an error in the CFD method, indicating the possibility of ML having a higher accuracy. However, category 3 includes cases where the algorithm had errors that should be fixed. Because the number of cases in category 2 (four cases) exceeded that in category 3 (two cases), it can be confirmed that DEC_{SVM} can provide more information than FFRGPR. Table 3 lists the accuracy, sensitivity, positive predictive value (PPV), and negative predictive value (NPV) for 20 cases. Accuracy is defined as the percentage of correctly guessed cases, for both positive and negative results by FFR $\geq$ 0.8. Sensitivity is defined as correctly guessed cases among $FFR_{EXP} \geq 0.8$ cases, while specificity is defined as correctly guessed cases among $FFR_{EXP} < 0.8$ cases. Also, PPV is defined as correctly guessed cases among $FFR_{GPR} \geq 0.8$ or $DEC_{SVM} = 0$ cases, while NPV is defined as correctly guessed cases among $FFR_{GPR} < 0.8$ or $DEC_{SVM} = 1$ cases.

The performance of FFR_{GPR} was not very different from that of FFR_{CFD}. However, the accuracy of DEC_{SVM} was slightly higher than that of FFR_{GPR} with higher specificity but lower sensitivity. Furthermore, both the PPV and NPV of DEC_{SVM} were higher than those of FFR_{GPR}.

Fig. 4 shows the error percentage with data index aligned by FFR_{GPR}. The error value was calculated by the difference between FFR_{EXP} and FFR_{GPR}. The average error percentage was 27.46% when $FFR_{EXP} < 0.75$ (4 cases), 3.80% when $0.75 \leq FFR_{EXP} < 0.85$ (6 cases), and 12.70% when $FFR_{EXP} \geq 0.85$ (10 cases).

Because the decision borderline, or where DEC_{EXP} value changes, was at $FFR_{EXP} = 0.8$, the most important region was when $0.75 \leq FFR_{EXP} < 0.85$. Note that the error percentage was the lowest in this region. Fig. 5 shows the relative weight factor of each features when the SVM model was trained. A higher weight factor indicates that the DEC_{SVM} is more affected by that feature.

Flow characteristics analysis

Further analysis of each category was performed in terms of the flow characteristics, and we analyzed two types of flow characteristics. The first type is related to secondary flow, which includes vorticity, helicity, swirling strength, and turbulence intensity; however, the second type is related to the wall shear, including wall shear stress (WSS), oscillatory shear index (OSI), and axial plaque stress (APS). Fig. 6 shows the correlation between flow features and FFR_{EXP}. The position between -1 and 0 is the proximal lumen, that between 0 and 1 is the center lumen, and that between 1 and 2.5 is the distal lumen. Most of the features had the highest correlation when the distance was near 1.0. The wall shear features had an overall lower correlation compared with the secondary flow features, and the swirling strength showed the highest correlation among other features. This confirms that flow energy loss by secondary flow was dominant compared with other wall shear features.

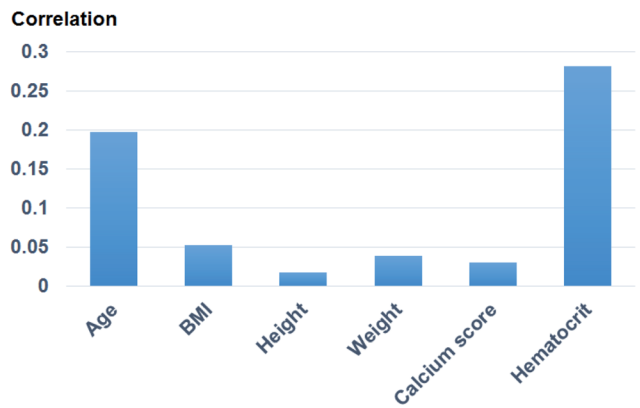

Fig. 9 Correlation of each biometric feature.

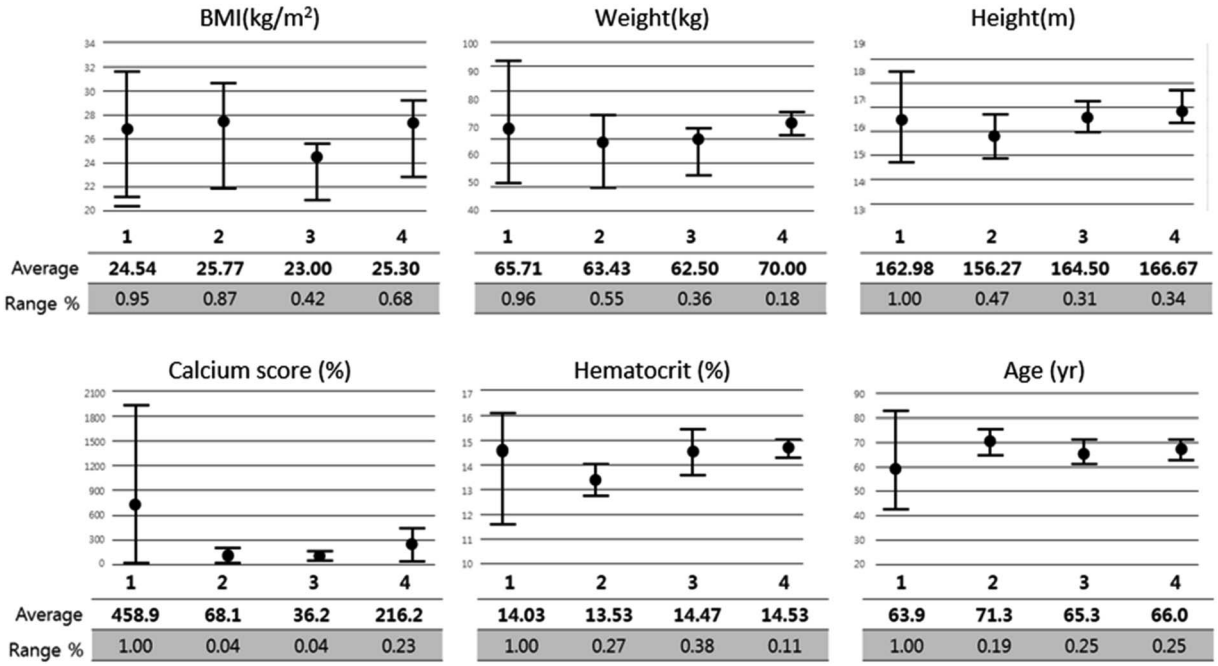

Fig. 10 Biometric features of 20 cases separated into four categories.

Fig. 7 shows pressure, vorticity, and WSS of 20 cases separated by four categories. Moreover, it shows the contours of pressure, vorticity, and WSS with sample cases from each category. In Fig. 7, it is important to note the range of values and not only the average value. If the range of a feature in category 2 or 3 is similar to that in categories 1 and 4, it indicates that the feature does not contribute to the mismatch. However, if this range is smaller in category 2 or 3, it indicates that the feature might be related to the mismatch and additional investigation is required. Fig. 8 shows that the FFR_{EXP}, vorticity, and OSI showed a smaller range in categories 2 and 3 compared with category 1.

Biometric parameter analysis

Fig. 9 shows the correlation between biometric features such as age, BMI, calcium score, and hematocrit. Fig. 10 shows each biometric feature of the 20 cases separated into four categories. As in the case of Fig. 7, the range difference in each category should be noted. Among all the features, hematocrit showed the highest correlation, followed by age. Note that the correlation of BMI was higher than that of height and weight. If the effects of height and weight were independent of each other, their correlation should have been higher than that of BMI because BMI is a function of height and weight. However, the higher correlation of BMI indicates that height and weight are dependent and should be merged with BMI for better analysis.

Conclusions

In this study, a two-step ML algorithm is introduced to estimate FFR and obtain DEC. By training the model with both a synthetic model and a patient model with the help of CFD, flow characteristics and biometric features could be used. Consequently, DEC_{SVM} was higher than FFR_{CFD} or FFR_{GPR}, which confirmed the potential of this algorithm to overcome the accuracy limitation compared with FFR_{CFD}.

There are still a few limitations that should be further studied to achieve a better model. The most critical limitation is that the quality and quantity of biometric features might not be enough. For example, while age or calcification is used to represent vessel stiffness, the exact vessel stiffness cannot be obtained unless it is measured directly. However, it is almost impossible to measure every FFR-related feature from every patient. Even the synthetic models used for amplifying the cases are not helpful for solving this problem because the features estimable by synthetic models are limited to CFD.

Also, the category 3 cases in the performance test result should be further analyzed and be eliminated. Category 3 means that DEC_{SVM} has poorly guessed even after the correct estimation of FFR_{GPR}. The cause of these errors are probably due to the overfitting problem of the SVM algorithm, but the cases used for performance test are yet not enough to fully analyze and correct this error. In future works, solving this problem and reducing category 3 cases is going to be the main objectives to improve the algorithm.

Regardless of these limitations, it was confirmed that the accuracy of the ML algorithm can surpass that of CFD. The ultimate goal of ML-based FFR should not only be a reduced calculation time but also obtaining a sufficiently high accuracy and practicality so as to replace the FFR_{EXP}.

Conflicts of interest

There are no conflicts to declare.

Acknowledgements

This work of Yong Woo Kim, Jung-Sun Kim, Jinyong Ha, and Joon Sang Lee was supported by the National Research Foundation of Korea (NRF) grant funded by the Korean government (NRF-2017M3A9E9073371). Also, The work of Hee-Jin Yu and Jongeun Choi was supported in part by the National Research Foundation of Korea (NRF) under Grant 2018R1A4A1025986 funded by the Korea government (MSIT). Young Woo Kim and Hee-Jin Yu contributed equally to this work as first authors. Also, Jongeun Choi and Joon Sang Lee contributed equally to this work as corresponding authors.

Notes and references

1 B. D. Bruyne and J. Sarma, *Heart*, 2008, **94**, 949–959.
2 P. A. Tonino, W. F. Fearon, B. De Bruyne, K. G. Oldroyd, M. A. Leesar, P. N. Ver Lee, P. A. MacCarthy, V. Marcel and N. H. Pijls, *J. Am. Coll. Cardiol.*, 2010, **55**, 2816–2821.
3 M. A. Mamas, S. Honer, E. Welch, A. Ashworth, S. Millington, D. Fraser, F. Fath-Ordoudabadi, L. Neyses and M. El-Omar, *J. Invasive Cardiol.*, 2010, **22**, 260–265.
4 G. Casella, M. Leibig, T. M. Scheile, R. Schrepf, V. Seeling, H. Stempfle, P. Erdin, J. Rieber, A. Konig, U. Siebert and V. Klauss, *Am. Heart J.*, 2004, **148**, 590–595.
5 A. Coenen, M. M. Lubbers, A. Kono, A. Dedic, R. G. Chelu, M. L. Dijkshoorn, F. J. Gijsen, M. Ouhlous, R. M. van Geuns and K. Nieman, *Radiology*, 2014, **274**, 674–683.
6 C. A. Taylor, A. F. Timothy and K. M. James, *J. Am. Coll. Cardiol.*, 2013, **61**, 2233–2241.
7 R. K. Tripathy, S. Mahanta and S. Paul, *RSC Adv.*, 2014, **4**, 9349–9355.
8 M. Khanmohammadi, K. Ghasemi and A. B. Garmarudi, *RSC Adv.*, 2014, **4**, 41484–41490.
9 A. Kihm, L. Kaestener, C. Wagner and S. Quint, *PLoS Comput. Biol.*, 2018, **14**, e1006278.
10 G. Kim, J. G. Lee, S. J. Kang, P. NNguen, D. Y. Kang, P. H. Leem J. M. Ahn, D. W. Park, S. W. Lee, Y. H. Kim, C. W. Lee, S. W. Park, and S. J. Park, *Intravascular Imaging and Computer Assisted Stenting and Large-Scale Annotation of Biomedical Data and Expert Label Synthesis*, 2018, pp. 73–81.
11 L. Itu, S. Rapaka, T. Passerini, B. Georgescu, C. Schwemmer, M. Schoebinger, T. Flohr, P. Sharma and D. Comaniciu, *J. Appl. Physiol.*, 2016, **121**, 42–52.
12 C. Tesche, C. N. Cecco, S. Baumann, M. Renker, T. W. McLaurin, T. M. Duguay, R. R. Bayer, D. H. Steinberg, K. L. Grant, C. Canstein, C. Schwemmer, M. Schobinger, L. M. Itu, S. Rapaka, P. Sharma and U. J. Schoepf, *Radiology*, 2018, **288**, 64–72.
13 X. Hu, M. Yang, L. Han and Y. Du, *Int. J. Cardiovasc. Imaging*, 2018, **34**, 1987–1996.
14 M. Chu, C. Birgelen, Y. Li, J. Westra, J. Yang, N. R. Holm, J. H. Reiber, W. Wijns and S. Tu, *Atherosclerosis*, 2018, **273**, 136–144.
15 S. S. Varghese and H. F. Steven, *J. Biomech. Eng.*, 2003, **125**, 445–460.
16 H. S. Lim, P. A. Tonino, B. De Bruyne, A. S. Yong, B. K. Lee, N. H. Pijls and W. F. Fearon, *Int. J. Cardiol.*, 2014, **177**, 66–70.
17 S. Li, X. Tang, L. Peng, Y. Luo, R. Dong and J. Liu, *Clin. Radiol.*, 2015, **70**, 476–486.
18 M. Renker, U. J. Schoepf, R. Wang, F. G. Meinel, J. D. Rier, R. R. Bayer, H. Mollmann, C. W. Hamm, D. H. Steinberg and S. Baumman, *Am. J. Cardiol.*, 2014, **114**, 1303–1308.
19 A. Asfaram, M. Ghaedi, M. H. Ahmadi Azqhandi, A. Goudarzi and M. Dastkhoon, *RSC Adv.*, 2016, **6**, 40502–40516.
20 Q. Li, Y. Yu, P. Zhou and H. J. Yan, *RSC Adv.*, 2017, **7**, 14701–14708.
21 Q. Mei, X. Wei, W. Sun, X. Zhang, W. Li and L. Ma, *RSC Adv.*, 2019, **9**, 12846–12853.
22 Y. L. Chen, *RSC Adv.*, 2014, **4**, 17908–17916.
23 J. Y. Moon, S. B. Choi, J. S. Lee, R. I. Tanner and J. S. Lee, *Phys. Rev. E*, 2019, **99**, 022607.
24 A. Purqon, *J. Phys.: Conf. Ser.*, 2017, **877**, 012035.
25 D. Y. Kang, J. M. Ahn, Y. W. Kim, J. Y. Moon, J. S. Lee, B. K. Koo, P. H. Lee, D. W. Park, S. J. Kang, S. W. Lee, Y. H. Kim, S. W. Park and S. J. Park, *Circ. Cardiovasc. Imaging*, 2018, **11**, 007087.
26 K. Govindaraju, G. N. Viswanathan, I. A. Badruddin, S. Kamangar, N. J. Salman and A. A. Al-Rashed, *Comput. Methods Biomech. Biomed. Eng.*, 2016, **19**, 1541–1549.
27 L. Zhang, Z. Jiang, J. Choi, C. Y. Lim, T. Maiti and S. Baek, *IEEE J. Biomed. Health*, 2019, **23**, 2537–2550.
28 H. N. Do, A. Ijaz, H. Gharahi, B. Zambrano, J. Choi, W. Lee and S. Baek, *IEEE Trans. Biomed. Eng.*, 2018, **66**, 609–622.
29 G. W. Colopy, S. J. Roberts and D. A. Clifton, *IEEE J. Biomed. Health*, 2018, **22**, 301–310.
30 S. I. Lee, B. Mortazavi, H. A. Hoffmann, D. S. Lu, C. Li, B. H. Paak, J. H. Garst, M. Razaghy, M. Espinal, E. Park, D. C. Lu and M. Sarrafzadeh, *IEEE J. Biomed. Health*, 2014, **20**, 91–99.
31 E. Byvatov and S. Gisbert, *Appl. Bioinf.*, 2003, **2**, 67–77.
32 T. T. Yao, J. L. Cheng, B. R. Xu, M. Z. Zhang, Y. Z. Hu, Ji. H. Zhao and X. W. Dong, *RSC Adv.*, 2015, **61**, 49195–49203.
33 S. Hanneke and K. Aryeh, *Theor. Comput. Sci.*, 2019, **796**, 99–113.
34 J. Chen and Y. Jieping, *Proceedings of the 25th international conference on Machine learning.*, 2008, pp. 136–143.
35 M. B. Kursa and W. R. Rudnicki, *J. Stat. Softw.*, 2010, **36**, 1–13.

